



# Adsorption, isolated electron/hole transport, and confined catalysis coupling to enhance the photocatalytic degradation performance

Junwei Yuan<sup>a</sup>, Hua Li<sup>a,b,\*</sup>, Guan Wang<sup>a</sup>, Cheng Zhang<sup>a</sup>, Yuxiang Wang<sup>a</sup>, LiuJun Yang<sup>a</sup>, Miaomiao Li<sup>a</sup>, Jianmei Lu<sup>a,b,\*</sup>

<sup>a</sup> College of Chemistry, Chemical Engineering and Materials Science, Collaborative, Innovation Center of Suzhou Nano Science and Technology, Soochow University, Suzhou, Jiangsu 215123, China

<sup>b</sup> National Center of International Research on Intelligent New Nanomaterials and Detection Technologies in Environmental Protection, Suzhou, Jiangsu 215123, China

## ARTICLE INFO

### Keywords:

Adsorption  
Confined catalysis  
Photocatalytic degradation  
Phenol  
H<sub>2</sub>O<sub>2</sub> generation

## ABSTRACT

A high photogenerated carrier efficiency and a minimal recombination rate are key factors in achieving high photocatalytic efficiency. Herein, N-doped carbon (NC) nanotubes and polyaniline (PANI) fibers are compounded around Ag<sub>3</sub>PO<sub>4</sub> nanoparticles to form a built-in electric field for electron-hole double transfer. Wrapping β-cyclodextrin (β-CD) around PANI fiber to isolate electron/hole composite channels is innovatively proposed. By reducing the recombination probability, more electrons can be transferred to the NC to realize a reduction of O<sub>2</sub> to H<sub>2</sub>O<sub>2</sub>. Additionally, the encapsulation of PANI fiber by β-CD can stabilize hole carriers, and enable phenol to be quickly transported to the confined space containing abundant hole carriers for rapid degradation. The obtained 3%CDP@Ag<sub>3</sub>PO<sub>4</sub>@NC catalyst's charge extraction rate is twice that of Ag<sub>3</sub>PO<sub>4</sub> and exhibits high photodegradation performance with 100% removal rate of 20 ppm phenol within 8 min under visible light, the performance of which is superior to currently Ag<sub>3</sub>PO<sub>4</sub> based catalysts reported.

## 1. Introduction

With the acceleration of human urbanization and industrialization, environmental deterioration and water pollution have become severe social problems. Phenol-containing wastewater produced from all walks of life seriously threatens human health [1,2]. Photocatalytic degradation technology, as a common wastewater purification technology to degrade phenolic pollutants using light irradiation, has attracted much attention [3,4]. Photocatalytic technology can degrade organic pollutants by only using light and does not produce secondary pollution, which makes it a promising clean technology [5]. However, at present, photocatalysts have some shortcomings, such as low concentration of photogenerated carriers, short lifetime, and high electron/hole recombination rate, which has seriously hindered the application of photocatalytic technology [6,7]. Therefore, achieving maximum electron/hole generation and minimum recombination has become the bottleneck in the photocatalytic field. Constructing a catalytic system that can not only efficiently generate photogenerated carriers, but also quickly isolate and transport holes and electrons would be the best way

to solve the abovementioned problems.

Several strategies have been used to study the maximum electron/hole generation and minimum recombination. Structure of heterojunction catalysts: Gao et al. constructed a facet heterojunction (FH) structure to prolong the lifetime of photogenerated electrons and achieved effective separation of electron-hole pairs in rutile TiO<sub>2</sub> [8]. Spatial separation system of photocarriers by conductive materials: Lin et al. constructed Ag<sub>3</sub>PO<sub>4</sub>@MWCNTs@PPy composite material, which transferred the photo-induced electrons of Ag<sub>3</sub>PO<sub>4</sub> to MWCNTs, and the photo-induced holes migrate to the surface of PPy, resulting in superior separation efficiency of photogenerated carriers and great enhancement of photocatalytic activity [9]. Atomic-level spatial separation of photogenerated carriers: Wang et al. developed a simple Cu-N<sub>4</sub> and C-S-C diatomic strategy, the isolated Cu-N<sub>4</sub> sites directly capture photogenerated electrons and the surrounding S atoms bear photo-generated holes in the polymeric carbon nitride, which facilitates the separation of photogenerated carriers and resulted in enhanced photocatalytic activity [10]. Ji and Wang et al. carried out the atomic confinement and coordination (ACC) strategy to realize the enrichment of electrons by

\* Corresponding authors at: College of Chemistry, Chemical Engineering and Materials Science, Collaborative, Innovation Center of Suzhou Nano Science and Technology, Soochow University, Suzhou, Jiangsu 215123, China.

E-mail addresses: [lihuaw@suda.edu.cn](mailto:lihuaw@suda.edu.cn) (H. Li), [lujm@suda.edu.cn](mailto:lujm@suda.edu.cn) (J. Lu).

<https://doi.org/10.1016/j.apcatb.2021.120892>

Received 8 September 2021; Received in revised form 28 October 2021; Accepted 31 October 2021

Available online 6 November 2021

0926-3373/© 2021 Elsevier B.V. All rights reserved.

single metal atoms on the carrier, which promoted the separation of electron-hole pairs for Enhanced Photocatalytic CO<sub>2</sub> Reduction [11,12].

Photoresponsive Ag<sub>3</sub>PO<sub>4</sub> has been widely used in the field of photocatalysis because of its high photooxidation efficiency, quantum conversion efficiency, good carrier mobility, and abundant surface active sites [13]. However, the high electron/hole recombination rate and photocorrosion limit the catalytic performance of Ag<sub>3</sub>PO<sub>4</sub> [14]. Yu and Zhu reported an improvement of its catalytic efficiency by adding g-C<sub>3</sub>N<sub>4</sub> or ZnO to form heterojunctions to change the carrier migration and thus prolong the carrier lifetime [15,16]. Yan and Li reported a promotion of the electron/hole transmission capacity by establishing an internal electric field in combination with conductive materials [17,18]. Highly toxic phenol wastewater is rarely used to evaluate the performance of photocatalytic materials because of its refractory characteristics [19,20]. Therefore, constructing a rapid and economical catalytic degradation system for low-concentration phenol wastewater has become a scientific problem that needs to be broken through urgently.

N-doped carbon (NC) and polyaniline (PANI) have been chosen as superior electron [15,16] and hole transmission carriers [21–23], respectively, in multicomponent photocatalyst systems. To isolate the electron/hole transmission channel to hinder their recombination, herein,  $\beta$ -CD was used to wrap the PANI fibers (here named as CDP) [24], which is expected to quickly transfer the photogenerated holes and prevent them from recombining with the outside electrons. In addition,  $\beta$ -CD can quickly adsorb phenol in the solution to its internal confinement space, so that the phenol and holes on the PANI fiber wire wrapped by  $\beta$ -CD contact at zero distance, thereby greatly accelerating the oxidative degradation of phenol.

Taking into account the above analysis, a three-component photocatalyst, CDP@Ag<sub>3</sub>PO<sub>4</sub>@NC, was constructed for maximization of the separation and isolation of photogenerated electrons/holes to achieve ultra-efficient photocatalytic performance with a 100% removal rate of 20 ppm phenol within 8 min under visible light, which, to the best of our knowledge, is superior to other materials with catalytic degradation rate for phenol to date (Table S2). This catalyst construction strategy, which isolates the transmission of electrons and holes and quickly adsorbs pollutants into the confined space for site-specific catalysis, provides the potential for accelerating the application of photocatalyst materials.

## 2. Materials and methods

### 2.1. Materials

Tris base was purchased from J&K scientific and dopamine hydrochloride from energy chemical. Silver acetate (CH<sub>3</sub>COOAg), ammonium persulfate ((NH<sub>4</sub>)<sub>2</sub>S<sub>2</sub>O<sub>8</sub>), ammonium chloride (NH<sub>4</sub>Cl), aniline, oxalic acid were obtained from Macklin.  $\beta$ -cyclodextrin ( $\beta$ -CD), phenol, catalase, 2,2,6,6-tetramethylpiperidine (TEMP), 2,2,6,6-Tetramethylpiperidine 1-oxyl (TEMPO) and  $\beta$ -carotene were purchased from TCI. Potassium permanganate (KMnO<sub>4</sub>), ethanol (CH<sub>3</sub>CH<sub>2</sub>OH), hydrochloric acid (37%), disodium hydrogen phosphate dodecahydrate (Na<sub>2</sub>HPO<sub>4</sub>·12 H<sub>2</sub>O) are all produced by Sinopharm Chemical Reagent Co. Ltd., China. All chemicals are used without further purification. Deionized water was used throughout the experiment.

### 2.2. Materials characterization

The surface morphology and element mapping of all samples was analyzed by scanning electron microscopy (SEM, Hitachi SU8230). Transmission electron micrographs of the samples were obtained by Transmission electron microscopy (TEM, Tecnai G20) and high-resolution TEM (HRTEM, Tecnai G2 F20). Shimadzu UV-3600 was used to measure the UV Vis spectra. Raman spectra were recorded by Confocal LabRAM HR800 spectrometer with a 633 nm laser as an excitation source. FLS920 fluorescence spectrophotometer and Edinburgh F1/FSTCSPC 920 spectrophotometer were used to obtain the

fluorescence spectrum. The X-ray powder diffraction (XRD) patterns were recorded by X'Pert-Pro MPD with Cu K $\alpha$  radiation. X-ray photoelectron spectroscopy (XPS) was obtained by ESCALAB MK II with Al-K $\alpha$ . The morphology of CDP was obtained by atomic force microscopy (AFM). The concentration of phenol was determined by high-performance liquid chromatography (HPLC, Agilent 1260). The transient photovoltage (TPV) signals were registered using a 1 GHz digital phosphor oscilloscope (MDO3102, Tektronix). Electron spin resonance (ESR, JEOL JES-X320) spectroscopy was used to investigate the free radical spin capture experiments using 2,2,6,6-tetramethylpiperidine (TEMP), 2,2,6,6-Tetramethylpiperidine 1-oxyl (TEMPO) under a central magnetic field (326 mT), microwave frequency (9.15 GHz), and microwave power (1 mW).

### 2.3. Preparation of the samples

**Synthesis of N doped carbon nanotubes.** N-doped carbon nanotubes were synthesized by the template method [25]. First, NH<sub>4</sub>Cl (1 mmol) and KMnO<sub>4</sub> (1 mmol) were dissolved in deionized water (30 mL), respectively. Then the solution was mixed and stirred for 10 min, and finally was poured into the Teflon-lined stainless steel autoclave. The autoclave was heated up to 200 °C and held for 24 h. The MnO<sub>2</sub> nanowires were obtained by centrifugation, washed with ethanol and deionized water, and drying overnight in a vacuum (60 °C).

MnO<sub>2</sub> (50 mg) nanowires were dispersed into a tris-buffer solution (10 mM, 200 mL) and ultrasonicated for 30 min. Then, 100 mg of dopamine hydrochloride was added to the above MnO<sub>2</sub> suspension, and magnetic stirring was carried out for 4 h. MnO<sub>2</sub> @PDA product was washed several times with ethanol and deionized water and dried in a vacuum at 60 °C.

As-prepared MnO<sub>2</sub> @PDA was annealed in N<sub>2</sub> flow at 500 °C for 3 h with a heating rate of 1 °C·min<sup>-1</sup>. And then the resulting MnO<sub>2</sub> @NC product was dispersed in oxalic acid (0.5 M, 40 mL) and stirred at 70 °C for 12 h to completely remove the MnO<sub>2</sub> template. Finally, N-doped carbon was obtained by centrifugation, washing with ethanol and deionized water several times, and drying in a vacuum (60 °C).

**Synthesis of cyclodextrin polyaniline complex.** Aniline (4.0 mmol) was added to 200 mL hydrochloric acid (1.0 M) aqueous solution containing  $\beta$ -CD (4.0 mmol). After the mixture was stirred at room temperature for 5 h, ammonium persulfate (4.0 mmol) was added and continuously reacted for another 10 h [24]. The precipitate was collected by filtration and washed with water several times. The dark-green powder was finally achieved by the freeze-dried method.

**Synthesis CDP@Ag<sub>3</sub>PO<sub>4</sub>@NC.** CDP@Ag<sub>3</sub>PO<sub>4</sub> @NC was synthesized by electrostatically driven self-assembly [26]. In short, 0.01 g NC was dispersed in 400 mL deionized water and underwent ultrasonic treatment for 1 h to give the NC suspension. Different amounts of CDP, 7.5 mL NC suspension and CH<sub>3</sub>COOAg (1.503 g) were mixed with 200 mL deionized water in a flask. After stirring the mixture at 40 °C for 12 h, Na<sub>2</sub>HPO<sub>4</sub>·12 H<sub>2</sub>O aqueous solution was dropped into the mixture at the rate of 0.1 mL·min<sup>-1</sup>, and then continuously react for 6 h. Finally, the crude compounds were washed with DI water and dried overnight at 60 °C in a vacuum oven. For comparison, pure Ag<sub>3</sub>PO<sub>4</sub> and Ag<sub>3</sub>PO<sub>4</sub> @NC were prepared under the same conditions as that of CDP@Ag<sub>3</sub>PO<sub>4</sub> @NC.

### 2.4. Electrochemical experiments

The photocurrent and electrochemical impedance of the samples were recorded in an electrochemical workstation (CHI 760E, Shanghai, China). Indium-tin oxide (ITO) electrodes coated with 5 mg photocatalysts served as the working electrode. In the photoelectrochemical test, the platinum sheet and the Ag/AgCl electrode were used as the counter electrode and the reference electrode, respectively. The electrolyte solution of Na<sub>2</sub>SO<sub>4</sub> (0.1 M) and the light source of a 300 W xenon lamp were utilized in this system.

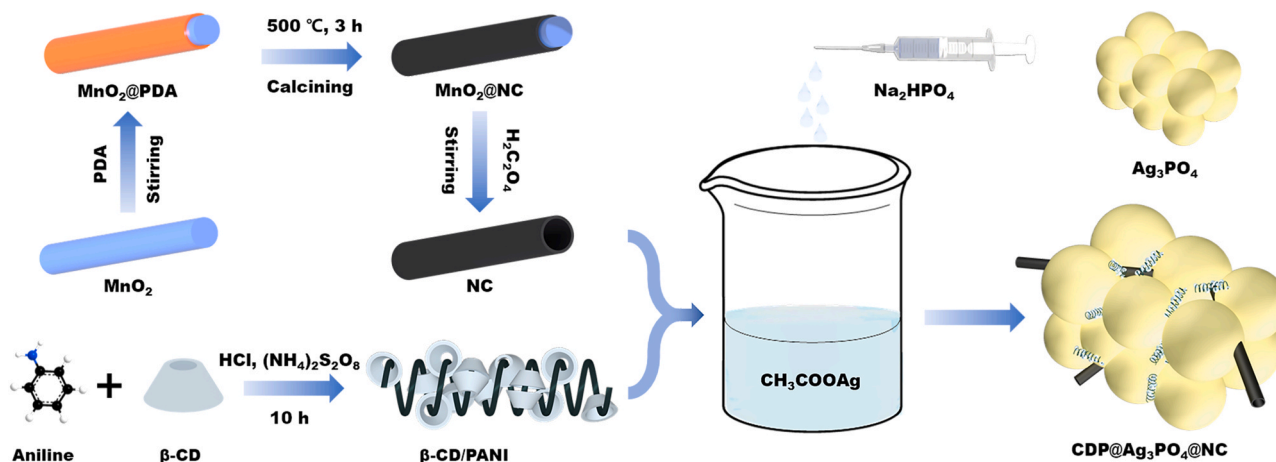


Fig. 1. Schematic illustration of the preparation route of CDP@Ag<sub>3</sub>PO<sub>4</sub> @NC.

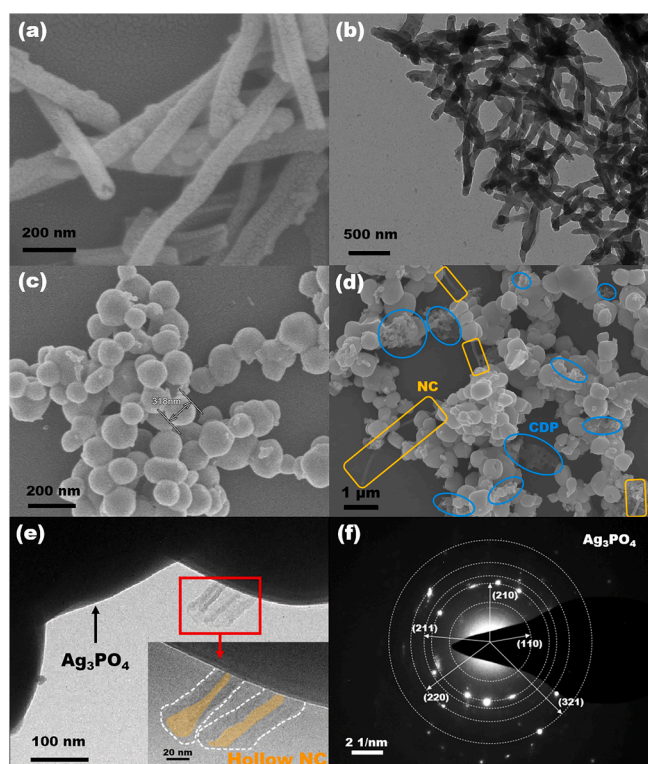


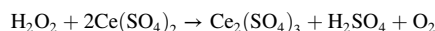
Fig. 2. (a) SEM images of NC, (b) TEM image of CDP. SEM images of (c) Ag<sub>3</sub>PO<sub>4</sub> and (d) CDP@Ag<sub>3</sub>PO<sub>4</sub> @NC, (e) TEM images of 3%CDP@Ag<sub>3</sub>PO<sub>4</sub> @NC and hollow NC, (f) SAED image of 3%CDP@Ag<sub>3</sub>PO<sub>4</sub> @NC.

## 2.5. Photocatalytic activity measurements

For Ag<sub>3</sub>PO<sub>4</sub>, Ag<sub>3</sub>PO<sub>4</sub> @NC, CDP@Ag<sub>3</sub>PO<sub>4</sub> @NC catalysts, their catalytic activities were tested by photooxidative degradation of phenol in water. The catalyst (50 mg) was placed into a photocatalytic reactor containing 100 mL of aqueous phenol solution with a concentration of 20 mg/L. The reactor was placed in the dark to allow it to reach adsorption equilibrium. After reaching the adsorption equilibrium, the photooxidation reactions were carried out under a 300 W xenon lamp (cut-off filter  $\lambda > 420$  nm). During the reaction, 1 mL of the solution is taken every 2 min and was subsequently filtered through membrane micro-filters with a pore size of 0.22  $\mu$ m. The phenol concentration of the pre-treated solution was detected by high-performance liquid chromatography (HPLC) measurement, which was performed at the

mobile phase of methanol and water (volume ratio: 60/40) with a 1 mL/min flow rate, and the detection wavelength is 275 nm. In addition, a photooxidation cycle experiment of phenol was further implemented to study the stability of CDP@Ag<sub>3</sub>PO<sub>4</sub> @NC.

**H<sub>2</sub>O<sub>2</sub> generation test of CDP@Ag<sub>3</sub>PO<sub>4</sub> @NC catalysts:** The catalyst (50 mg) was placed in a photocatalytic reactor containing 100 mL of deionized water under a 300 W xenon lamp (cut-off filter  $\lambda > 420$  nm). 0.05 M NaOH and 0.01 M EDTA solution were utilized as stabilizers to prevent H<sub>2</sub>O<sub>2</sub> from decomposing. The hydrogen peroxide concentration can be monitored through titration with a standard cerium sulfate solution (Ce(SO<sub>4</sub>)<sub>2</sub>), as reported [27]:



The quantitative calculation of H<sub>2</sub>O<sub>2</sub> is conducted by the absorption reduction value of the UV spectrum (read between 240 and 400 nm).

## 3. Results and discussion

### 3.1. Morphological and structure characterization

The preparation route of CDP@Ag<sub>3</sub>PO<sub>4</sub> @NC is illustrated in Fig. 1. Atomic force microscopy (AFM), scanning electron microscopy (SEM), transmission electron microscopy (TEM), and high-resolution transmission electron microscopy (HRTEM) were used to observe the morphology and microstructure of the synthetic samples. The AFM image of the insulated wire CDP (Fig. S1) shows that the PANI strung with  $\beta$ -CD helically formed fibrous structure with a size of 4 nm  $\times$  22 nm. The SEM image of the NC hollow tube, Ag<sub>3</sub>PO<sub>4</sub> and the TEM image of pure CDP are shown in Fig. 2a, c, and b, respectively. After blending with CDP and NC, the sedimentary Ag<sub>3</sub>PO<sub>4</sub> tightly adhered to them owing to the strong electrostatic force between the positively charged CDP, Ag<sup>+</sup> and the negatively charged NC, PO<sub>4</sub><sup>3-</sup> (Fig. S2), where the prepared CDP had a more positive charge than the purchased PANI. The SEM images in Fig. 2d confirmed that the Ag<sub>3</sub>PO<sub>4</sub> particles grew along the CDP and NC nanotubes with good contact. The hollow structure of the NC on Ag<sub>3</sub>PO<sub>4</sub> (Fig. 2e) was also observed through HRTEM and the diffraction data (Fig. 2f) measured by selected area electron diffraction (SAED) were consistent with the standard card JCPDS No.06-0505. The element surface distribution diagram of CDP@Ag<sub>3</sub>PO<sub>4</sub> @NC in Fig. S3 shows that the N element was evenly distributed over the whole catalyst.

X-ray powder diffraction (XRD) was used to characterize the phase purity and crystallinity of CDP@Ag<sub>3</sub>PO<sub>4</sub> @NC. Fig. 3a shows that the XRD diffraction peaks of CDP@Ag<sub>3</sub>PO<sub>4</sub> @NC agreed with those of Ag<sub>3</sub>PO<sub>4</sub>, which indicated no change in the diffraction peak of Ag<sub>3</sub>PO<sub>4</sub> by the introduction of CDP and NC. By comparison with the standard card



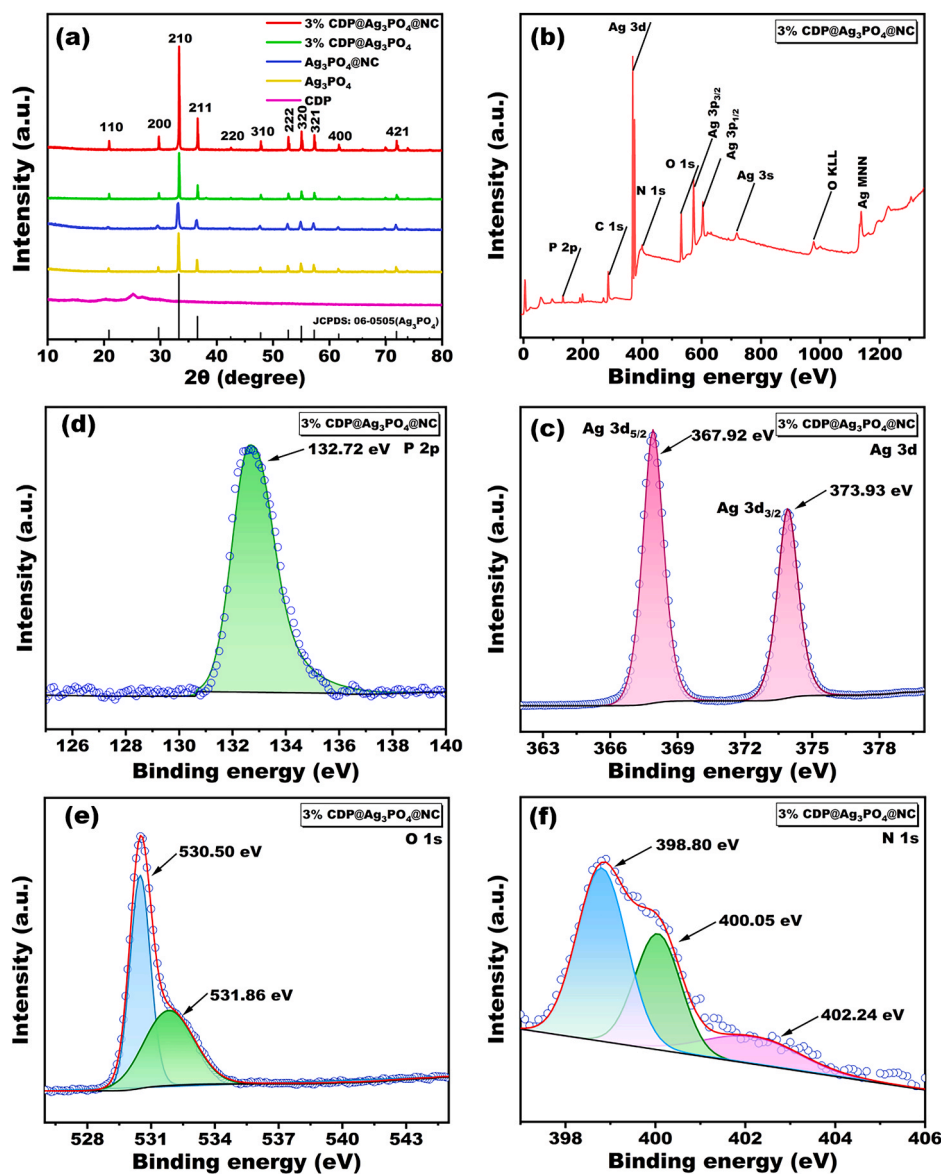


Fig. 3. (a) XRD pattern of as-prepared samples, (b) XPS survey spectra, high-resolution XPS spectrum of (c) Ag 3d, (d) P 2p, (e) O 1s, and (f) N 1s.

JCPDS No.06-0505, the peaks at  $20.9^\circ$ ,  $29.8^\circ$ , and  $52.8^\circ$  corresponded to the crystal planes of {110}, {200}, and {222}, respectively. Thus, the stronger XRD diffraction peaks at (110) and (200) after the combination with CDP and NC indicated that more of the crystal plane of  $\text{Ag}_3\text{PO}_4$  was exposed [26]. The diffraction peak intensity ratio at (222) to (110) of  $\text{CDP@Ag}_3\text{PO}_4\text{@NC}$  was 3.82, which was much higher than the 1.51 of  $\text{Ag}_3\text{PO}_4$  and 1.7 of  $\text{Ag}_3\text{PO}_4\text{@NC}$  [28]. These results demonstrated that the incorporation of CDP can effectively increase the exposure of crystal faces with high surface energy and achieve more and higher surface active sites, which will lead to improved photocatalytic performances.

XPS was performed on the  $3\%\text{CDP@Ag}_3\text{PO}_4\text{@NC}$  to determine the chemical bonds. The main element (Ag, P, O, C, N) peaks in  $3\%\text{CDP@Ag}_3\text{PO}_4\text{@NC}$  were all obtained in the XPS spectrum, as shown in Fig. 3b. The peaks at 367.92 eV and 373.93 eV were attributed to Ag 3d<sub>5/2</sub> and Ag 3d<sub>3/2</sub> orbitals (Fig. 3c). The peak at 132.72 eV was assigned to the P 2p orbital (Fig. 3d). Compared with pure silver phosphate (Fig. S4a, S4b), the binding energies of Ag and P in the composite were shifted in the positive direction, which indicated that  $\text{Ag}_3\text{PO}_4$  decreases the electron density due to the electron transfer to NC [29]. The O 1s exhibited two peaks at binding energies of 530.50 eV and

531.86 eV, which corresponded to the crystalline oxygen and surface oxygen of  $\text{Ag}_3\text{PO}_4$  (Fig. 3e) [30]. The C 1s binding energy split into two peaks at 284.79 eV and 286.10 eV (Fig. S4c), where the 284.79 eV peak was assigned to  $\text{sp}^2$  hybridized carbon and that at 286.10 eV was assigned to the C-O bond and hydroxyl carbon [25]. As shown in Fig. 3f, the N 1s peak was divided into three peaks at 398.80 eV, 400.05 eV, and 402.24 eV, which were attributed to the C-N bond, -NH- (benzylamine), and positively charged nitrogen ( $-\text{HN}^+$  and  $-\text{HN}^+=$ ) [25,31,32], respectively. The above results confirmed that the C and N in CDP and NC formed interface interactions with  $\text{Ag}_3\text{PO}_4$ , which provided a channel for carrier transmission.

The Fourier infrared spectra of CDP,  $\text{Ag}_3\text{PO}_4$ , and  $3\%\text{CDP@Ag}_3\text{PO}_4\text{@NC}$  are shown in Fig. S7a. The peaks of PANI at  $1562\text{ cm}^{-1}$  (quinone ring C=C and C=N stretching mode) and  $1489\text{ cm}^{-1}$  (benzene ring C=C and C=N stretching mode) indicated that PANI was in a conductive state. The peaks at  $1289\text{ cm}^{-1}$  and  $1232\text{ cm}^{-1}$  were assigned to C-N bonds in PANI [33]. The observed PANI peaks in  $3\%\text{CDP@Ag}_3\text{PO}_4\text{@NC}$  confirmed the successful incorporation of CDP. Compared with the raw material, the spectra of the composite presented a weak blue-shift. The results indicated the coordination tendency between the transition



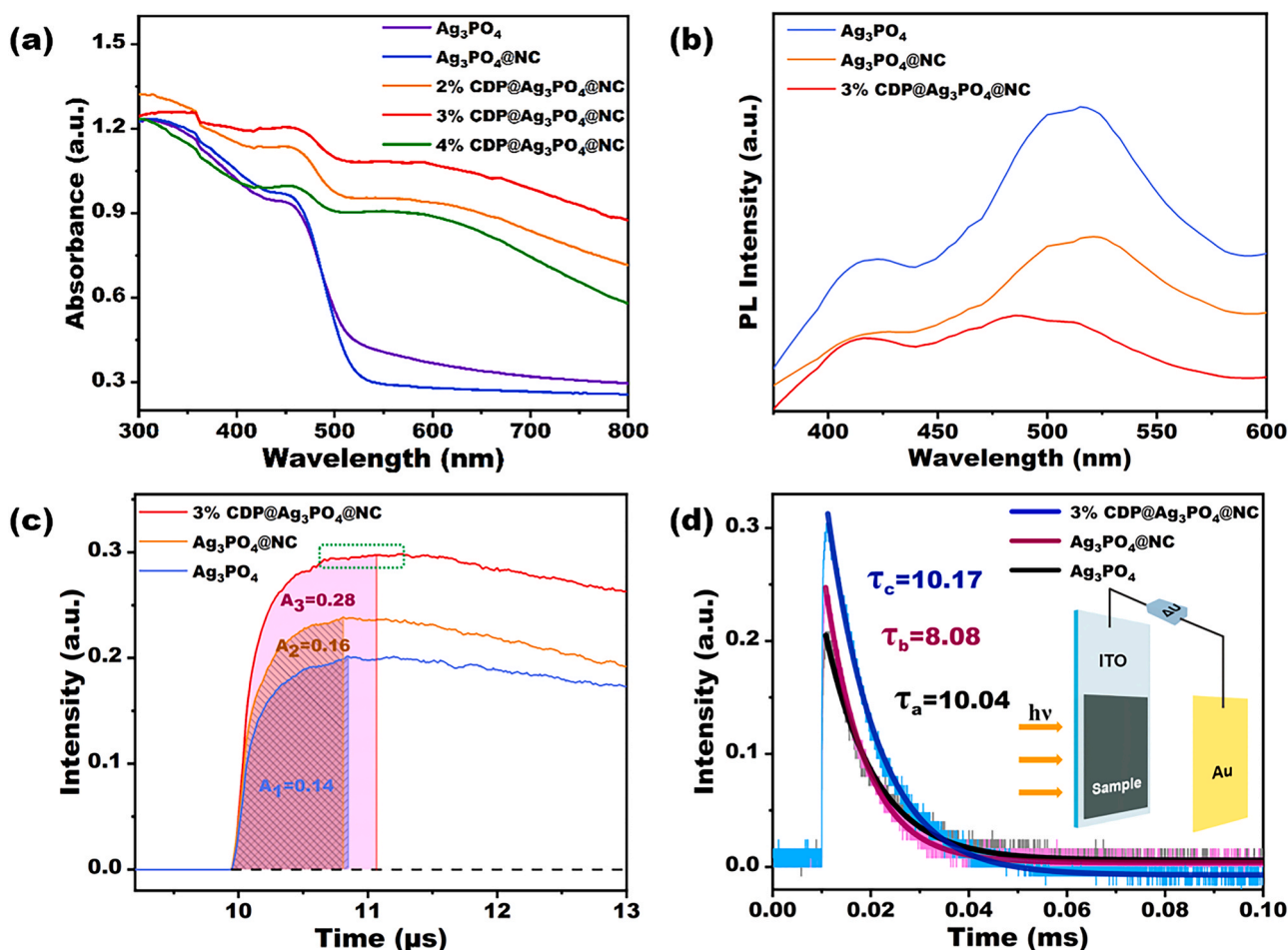


**Fig. 4.** (a) UV-vis absorption spectra, (b) PL spectra, (c-d) The transient photovoltage (TPV) of  $\text{Ag}_3\text{PO}_4$ ,  $\text{Ag}_3\text{PO}_4 @ \text{NC}$  and 3%CDP@ $\text{Ag}_3\text{PO}_4 @ \text{NC}$ . A is the amount of charge extracted from the catalyst and  $\tau$  is the time attenuation constants.

metal Ag and the nitrogen atoms on PANI, which was useful to carriers transfer and acquire better photocatalytic performance [34].

Raman spectroscopy further confirmed the interaction in CDP@ $\text{Ag}_3\text{PO}_4 @ \text{NC}$  (Fig. S7b). The strong vibration absorption at  $911 \text{ cm}^{-1}$  was attributed to the terminal oxygen of the phosphate group in  $\text{Ag}_3\text{PO}_4$ . The Raman peak at  $1166 \text{ cm}^{-1}$  was the bending vibration of the C-H bond, while the peaks at  $1468 \text{ cm}^{-1}$  and  $1592 \text{ cm}^{-1}$  were the vibration modes of the C=N bending of the quinoid ring and C-C stretching of the benzenoid rings [35], respectively. After the addition of CDP in  $\text{Ag}_3\text{PO}_4 @ \text{NC}$ , all the peaks are enhanced, which was explained by the stretching of the conjugate of PANI. Furthermore, a new peaks appeared, assigned to C-N<sup>+</sup> vibration of the quinoid ring ( $1333 \text{ cm}^{-1}$ ). The above results revealed that CDP tended to form a more conjugated structure with  $\text{Ag}_3\text{PO}_4$  [34,36]. The peaks of NC at  $1354 \text{ cm}^{-1}$  and  $1583 \text{ cm}^{-1}$  corresponded to the D and G bands. However, the D band peak was significantly weakened after incorporating NC into  $\text{Ag}_3\text{PO}_4$ , which showed that more amorphous and disordered carbons ( $\text{sp}^3$ ) were transformed into graphitic carbons ( $\text{sp}^2$ ). That is, NC and  $\text{Ag}_3\text{PO}_4$  were able to interact strongly with each other to facilitate photogenerated electron transmission [37].

### 3.2. Optical and electrochemical properties

Ultraviolet/visible diffuse reflectance spectroscopy (DRS) was used to determine the optical properties of all samples. As shown in Fig. 4a, all the samples showed strong optical absorption properties at the absorption wavelength ( $\leq 500 \text{ nm}$ ). Compared with  $\text{Ag}_3\text{PO}_4$ , the band gap of  $\text{Ag}_3\text{PO}_4 @ \text{NC}$  becomes wider (Fig. S6a, S6b) and the blue shift of UV

absorption becomes narrower, which can be explained by the quantum confinement effect. This is due to that the doping of NC avoids the agglomeration of  $\text{Ag}_3\text{PO}_4$  during the growth process, and obtains smaller  $\text{Ag}_3\text{PO}_4$  particles [38]. Conversely, the incorporation of CDP into  $\text{Ag}_3\text{PO}_4 @ \text{NC}$  enhanced the absorption intensity and broadened the absorption range significantly. Among all the samples doped with different amounts of CDP, 3%CDP@ $\text{Ag}_3\text{PO}_4 @ \text{NC}$  exhibited the best optical absorption performance.

The bandgap ( $E_g$ ) of the sample was calculated using the following Kubelka-Munke equation:

$$\alpha h\nu = A(h\nu - E_g)^{n/2} \quad (1)$$

where  $\alpha$ ,  $h$ ,  $\nu$ ,  $A$ , and  $E_g$  designate the absorption coefficient, Planck constant, light frequency, proportionality constant, and bandgap energy, respectively. Considering that  $\text{Ag}_3\text{PO}_4$  is an indirect semiconductor,  $n$  should be 4, thus,  $(\alpha h\nu)^2$  versus  $(h\nu)$  for  $\text{Ag}_3\text{PO}_4$  is shown in (Fig. S6a) and the bandgap ( $E_g$ ) of the sample was calculated to be 2.41 eV, which is similar to the previously published literature. The valence band ( $E_{VB}$ ) of  $\text{Ag}_3\text{PO}_4$  was 2.78 eV (Fig. S6c) based on the XPS data. Thus, the conduction band of  $\text{Ag}_3\text{PO}_4$  was calculated to be 0.37 eV [39], according to the following equation:

$$E_{CB} = E_{VB} - E_g \quad (2)$$

In addition, Mott-Schottky (MS) analysis of  $\text{Ag}_3\text{PO}_4$  was also performed and shown as typical n-type semiconductors with overall positive slopes. The applied potential was 0.18 eV (vs. saturated calomel electrode), as shown in Fig. S6d. The flat band potential was determined

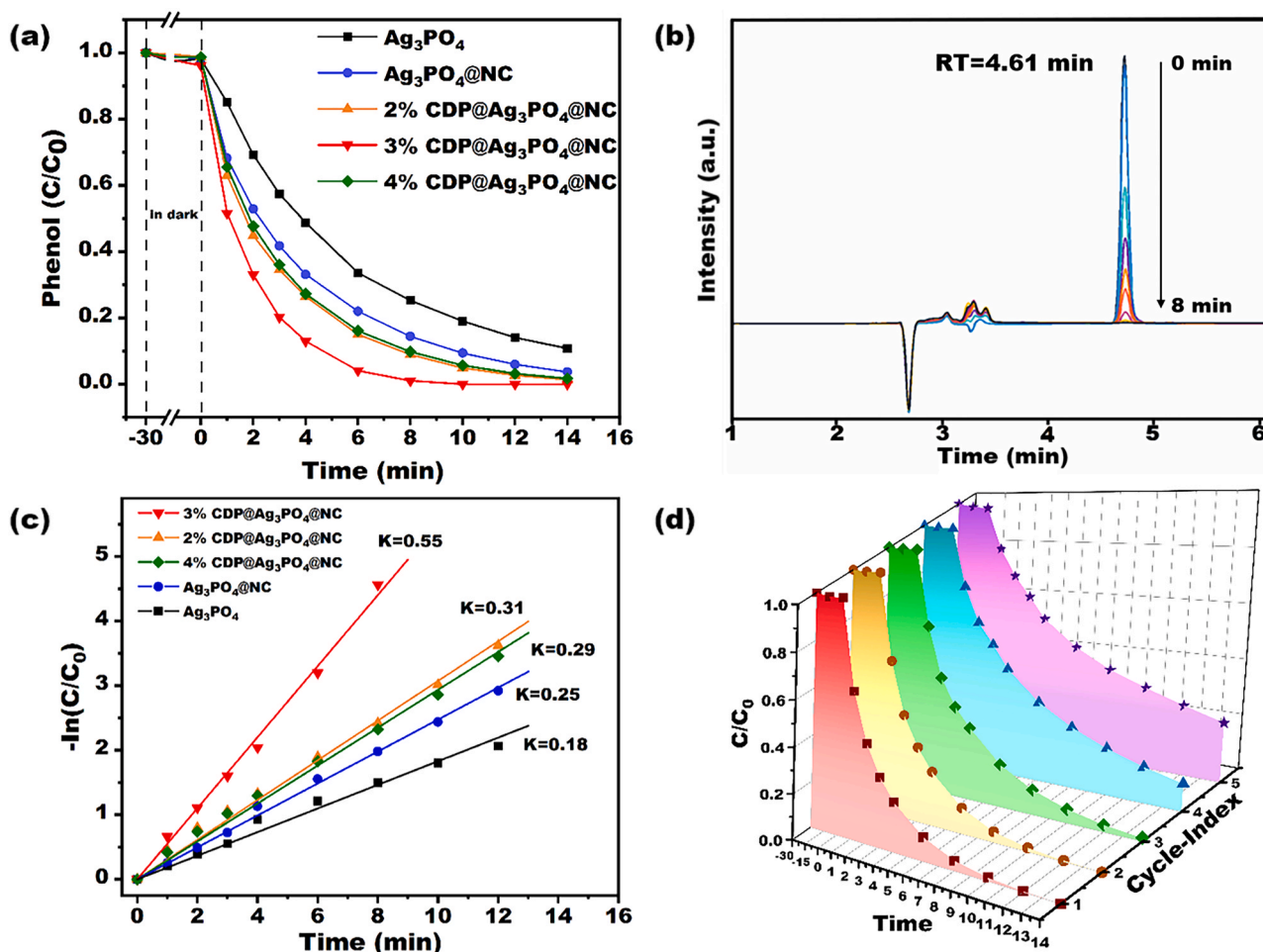


Fig. 5. (a) Photocatalytic activities of as-prepared samples for phenol removal under visible-light irradiation, (b) HPLC chromatograms of phenol degradation over 3%CDP@Ag<sub>3</sub>PO<sub>4</sub> @NC, (c) Kinetic rate constants (min<sup>-1</sup>) of these catalysts, (d) Cyclic photocatalytic experiments over 3%CDP@Ag<sub>3</sub>PO<sub>4</sub> @NC.

to be 0.15 eV, being equal to 0.39 eV versus normal hydrogen electrode (NHE) [30].

Cyclic voltammetry tests further determined the highest occupied molecular orbital (HOMO) and the lowest unoccupied molecular orbital (LUMO). As shown in Fig. S6e, the LUMO energy level can be calculated based on the following formula:

$$E_{\text{LUMO}} = -(E_{\text{red}} + 4.8 - E_{(\text{Fc}/\text{Fc}^+)}) \text{ eV} \quad (3)$$

$$E_{\text{NHE}} = -E_{\text{AVS}} - 4.5 \text{ eV} \quad (4)$$

where  $E_{\text{LUMO}}$ ,  $E_{\text{red}}$ , and  $E_{(\text{Fc}/\text{Fc}^+)}$  represent the LUMO energy level potential, reduction potential, and ferrocene/ferrocenium couple potential, respectively. Converting the reference electrode from the absolute vacuum scale (AVS) to the NHE (Eq. 4), the LUMO energy level was calculated to be -0.89 eV. The bandgap of CDP was calculated by Eq. (1) to be 2.86 eV (Fig. S6g), so its HOMO energy level was 1.97 eV [40].

Photoluminescence (PL) and photoelectrochemical tests were implemented to characterize the charge separation and carrier mobility performance. As shown in Fig. 4b, pure Ag<sub>3</sub>PO<sub>4</sub> had a strong emission peak near 510 nm originating from the rapid recombination of photo-generated electrons and holes. Compared with Ag<sub>3</sub>PO<sub>4</sub>, the fluorescence emission peak of the materials with NC and CDP was significantly weakened. Especially, the 3%CDP@Ag<sub>3</sub>PO<sub>4</sub> @NC had the weakest emission which demonstrated that the  $\beta$ -CD encapsulating PANI obviously obstructed recombination of the photogenerated carrier. The better fluorescence quenching and promising improved Ag<sub>3</sub>PO<sub>4</sub> photocatalytic performance were explained by the enhanced transfer of

electrons/holes with the assistance of the conductive materials NC and CDP[41].

The transient photovoltage (TPV) experiment was carried out to study the process of carrier generation and recombination. It can be seen from Fig. 4c that the electron extraction rate of 3%CDP@Ag<sub>3</sub>PO<sub>4</sub> @NC is the highest, which is twice that of Ag<sub>3</sub>PO<sub>4</sub>, indicating that the establishment of electron-hole double transfer channels significantly enhances the extraction of photo-generated carriers in Ag<sub>3</sub>PO<sub>4</sub>. Meanwhile, the long stationary time of the photovoltage can be observed in the 3% CDP@Ag<sub>3</sub>PO<sub>4</sub> @NC sample, which is caused by the fact that the electron cannot recombine with the hole isolated by  $\beta$ -CD. These effectively weaken the escape of the photogenerated electrons and stimulate them to participate in the reaction. Fig. 4d is the TPV curves of different samples, which shows the 3%CDP@Ag<sub>3</sub>PO<sub>4</sub> @NC decays more slowly and gently, indicating a slow combination of charges and enhancing photogenerated carrier transport with double transfer [42]. Therefore, CDP and NC enable Ag<sub>3</sub>PO<sub>4</sub> to equip with the best photo-generated carrier extraction and utilization performance.

As shown in Fig. S8a, the photocurrent of the 3%CDP@Ag<sub>3</sub>PO<sub>4</sub> @NC catalyst was considerably higher than that of the pure Ag<sub>3</sub>PO<sub>4</sub> catalyst, which showed that the high-efficiency conductors, NC and CDP, enhanced the spatial separation of photogenerated electrons and holes. So the double transfer of electron-hole insulation promoted the rapid transfer and separation of photogenerated charges leading to enhanced catalytic performances [43,44]. Furthermore, EIS was performed to verify the transfer and separation kinetics of the photogenerated charge carriers. The 3%CDP@Ag<sub>3</sub>PO<sub>4</sub> @NC had the smallest arc radius

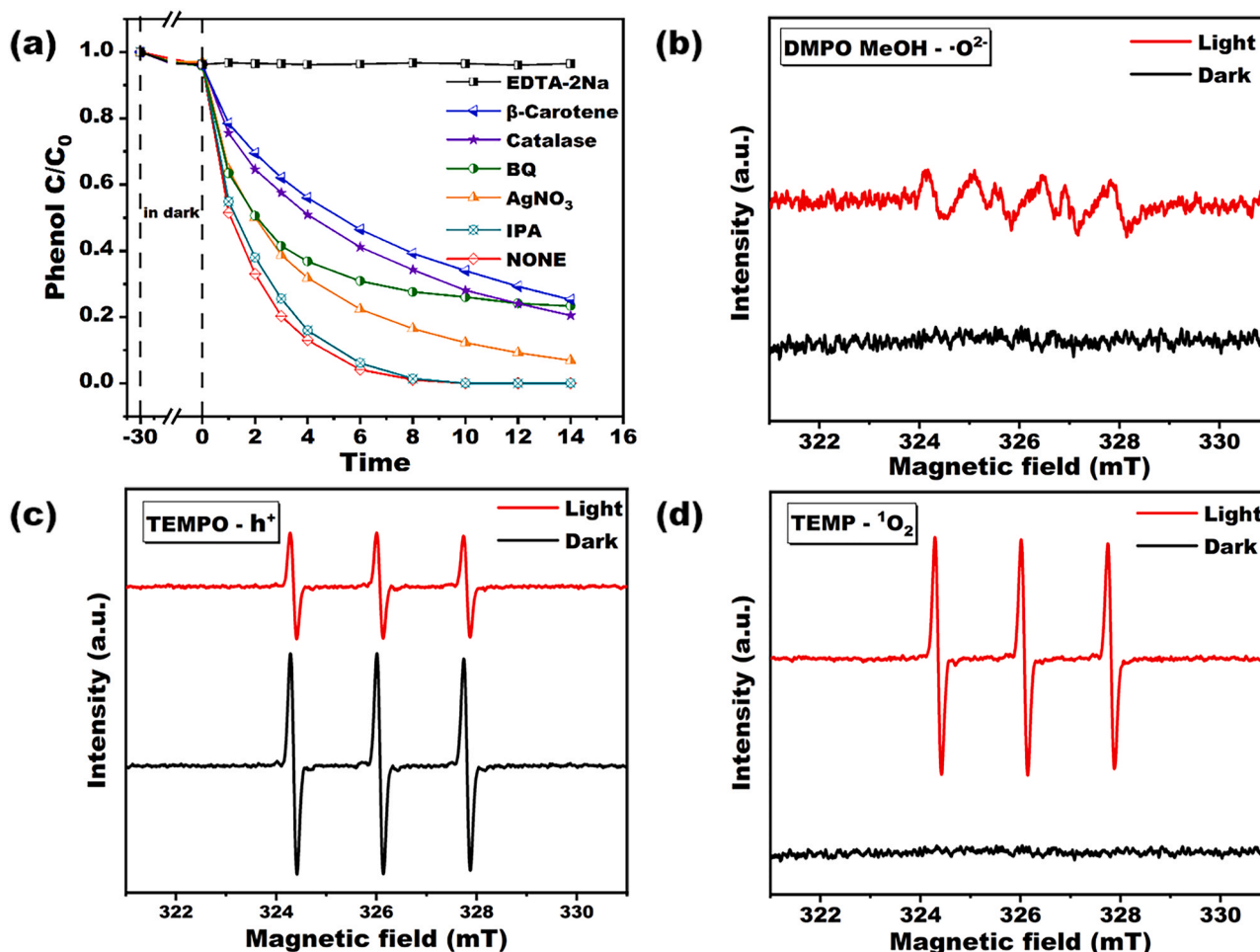


Fig. 6. (a) Photocatalytic degradation of phenol using 3%CDP@Ag<sub>3</sub>PO<sub>4</sub>@NC with different scavengers, (b) DMPO-·O<sub>2</sub><sup>-</sup>, (c) TEMPO-h<sup>+</sup>, (d) TEMP-<sup>1</sup>O<sub>2</sub> ESR spectra of 3%CDP@Ag<sub>3</sub>PO<sub>4</sub>@NC under irradiation.

(Fig. S8b), which corresponded to the lowest interface charge transfer resistance and stronger carrier mobility. These attributed to the efficient transfer of photogenerated electrons/holes to NC and CDP [45,46], so the catalyst possessed predictably superior photocatalytic performance.

### 3.3. Photocatalytic activity and recyclability

Herein, the oxidative degradation of phenol under visible light was used as a model reaction. The photocatalytic activity of the different samples was evaluated in detail without pH adjustment or oxidant addition. The phenol content in the solution was determined by high-performance liquid chromatography (HPLC). The pollutant-catalyst mixture solution was first stirred in the dark for 30 min to achieve adsorption/desorption equilibrium, and then placed under visible light before the catalytic reaction. As shown in Fig. 5a, with NC intensifying the property of Ag<sub>3</sub>PO<sub>4</sub>, the addition of CDP resulted in the optimally catalytic performance of the sample. By testing the catalytic performance of different CDP additions, it was found that 3%CDP@Ag<sub>3</sub>PO<sub>4</sub>@NC was able to remove phenol in 8 min (Fig. 5b), which resulted from the maximumly isolating transfer of photogenerated electrons/holes in Ag<sub>3</sub>PO<sub>4</sub> with the assistance of NC and CDP. To have a quantitative analysis of the photooxidation degradation process of phenol, the degradation kinetic curves of different catalysts were obtained and compared. It was found that the curves of the photooxidation degradation of phenol showed a linear relationship, which conformed to the first-order reaction kinetic equation:

$$-\ln(C/C_0) = kt \quad (5)$$

where  $C$  is the current pollutant concentration, and  $C_0$  is the initial pollutant concentration, while  $k$  is the reaction kinetic constant and  $t$  is the photodegradation reaction time. By contrast, the degradation rate of 3%CDP@Ag<sub>3</sub>PO<sub>4</sub>@NC of 0.55 was remarkably higher than that of Ag<sub>3</sub>PO<sub>4</sub>@NC (0.25) and Ag<sub>3</sub>PO<sub>4</sub> (0.18) (Fig. 5c), which indicated that 3%CDP@Ag<sub>3</sub>PO<sub>4</sub>@NC had the best photocatalytic performance. In addition, 3%CDP@Ag<sub>3</sub>PO<sub>4</sub>@NC still exhibited a degradation efficiency of 78% under visible light for 14 min even after five degradation cycles (Fig. 5d). The weakening of catalytic performance is mainly caused by the loss of catalyst and the slight photo-corrosion behavior of Ag<sub>3</sub>PO<sub>4</sub> (Fig. S5).

Different free radical trapping experiments were also performed to study the production of reactive species under visible light. During the photooxidation reaction of phenol, EDTA-2Na, β-carotene, catalase, BQ, AgNO<sub>3</sub>, and IPA were added separately to capture h<sup>+</sup>, <sup>1</sup>O<sub>2</sub>, ·O<sub>2</sub><sup>-</sup>, e<sup>-</sup>, ·OH. As shown in Fig. 6a, almost no catalytic degradation performance was observed with the addition of EDTA-2Na, which showed that strong holes are the most crucial active material for oxidative degradation of phenol. In contrast, the addition of β-carotene, catalase, and BQ considerably slowed down the catalytic rate, which confirmed that singlet oxygen (<sup>1</sup>O<sub>2</sub>), H<sub>2</sub>O<sub>2</sub>, and ·O<sub>2</sub><sup>-</sup> are also main catalytically active substances. Furthermore, the addition of AgNO<sub>3</sub> reduced the catalytic rate of the catalyst, which indicated that electrons also play a vital role in the catalysis process.

For further investigation of the related reactive species generated in



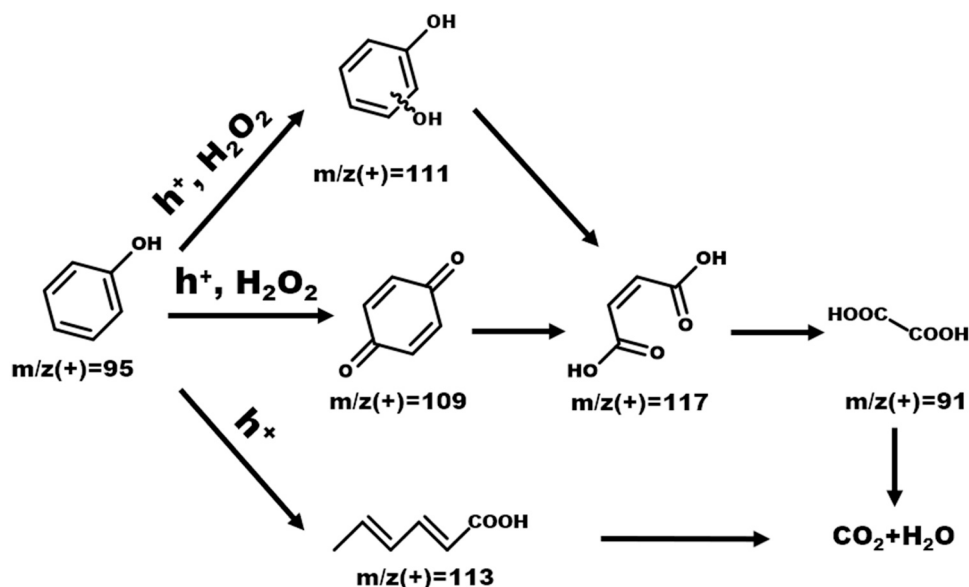


Fig. 7. Proposed phenol photodegradation pathways of 3%CDP@Ag<sub>3</sub>PO<sub>4</sub> @NC under visible-light illumination.

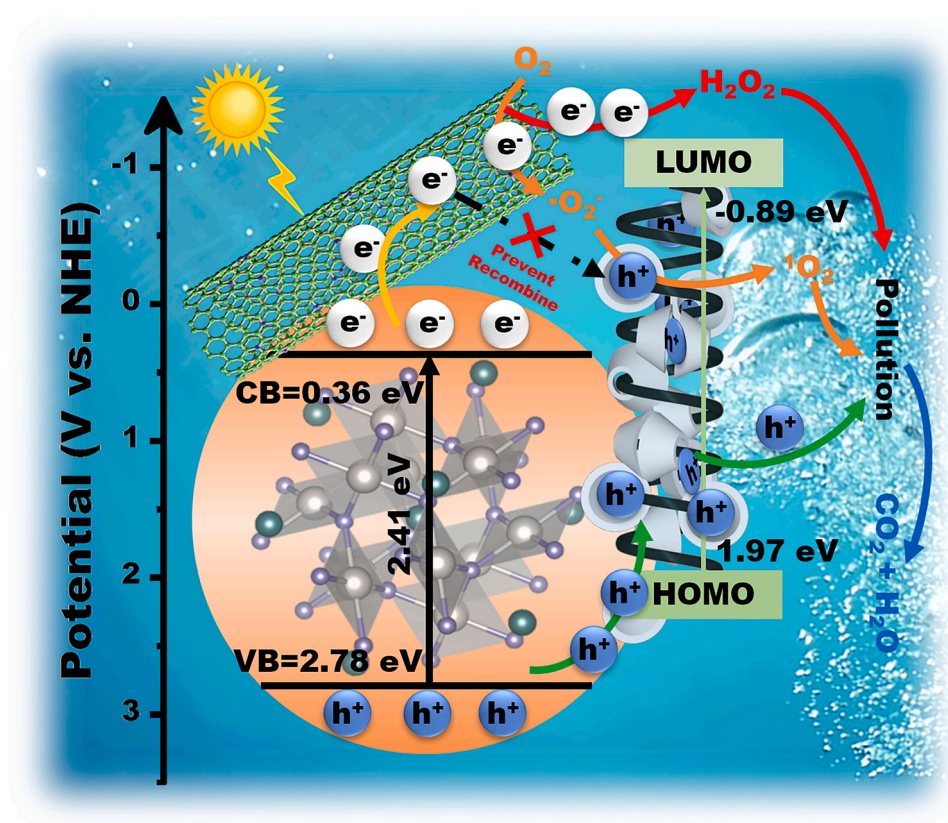


Fig. 8. Schematic mechanism of the phenol photocatalytic degradation by CDP@Ag<sub>3</sub>PO<sub>4</sub> @NC.

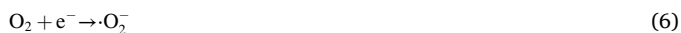
the photocatalytic process, the electron spin resonance (ESR) measurement was carried out. An ESR signal of DMPO- $O_2^{\cdot-}$  was observed after visible-light irradiation (Fig. 6b), which proved that these samples could generate  $O_2^{\cdot-}$  in the photocatalytic process [47]. TEMPO was used to capture  $h^+$ , and the TEMPO signal was greatly reduced under light (Fig. 6c), which indicated that many holes were generated by the catalyst. TEMP was used to capture  $^1O_2$ , and a strong peak appeared after visible-light irradiation revealed the presence of  $^1O_2$  (Fig. 6d) [48, 49]. Then, the water was photolyzed in an air atmosphere, and the

production of  $H_2O_2$  (Fig. S10b) with the reaction time was monitored according to the change in the absorbance of  $Ce^{IV}$  (Fig. S10a). Under the airtight photocatalytic reaction with the protection by oxygen-free argon, the UV absorption exhibited no change (Fig. S10c) after the  $Ce(SO_4)_2$  titration reaction solution confirmed no generation of  $H_2O_2$ , which proved that  $H_2O_2$  was produced by the two-electron reduction of oxygen.

LC-MS and TOC were used to detect intermediates generated during the photodegradation process (Fig. 7, Fig. S11, Fig. S12). Phenol

degradation was proposed to occur via two pathways: one is that phenol forms Benzenediol ( $m/z(+)=111$ ) or hydroquinone ( $m/z(+)=109$ ) under the action of  $h^+$  and  $H_2O_2$ . And they are then oxidized by  $h^+$  and  $O_2^-$  to produce Maleic ( $m/z(+)=117$ ), which can be further decomposed into oxalic acid ( $m/z(+)=91$ ). The other is that phenol is directly oxidized by  $h^+$  to form (2E,4E)-hexa-2,4-dienoic acid ( $m/z(+)=113$ ), which and oxalic acid ( $m/z(+)=91$ ) are eventually oxidized to  $CO_2$  and  $H_2O$ .

Based on the above experiment results and analysis, we proposed the following mechanism of the CDP@Ag<sub>3</sub>PO<sub>4</sub>@NC catalyst to degrade phenol (Fig. 8). a) First, the electrons of Ag<sub>3</sub>PO<sub>4</sub> transfer from the valence band to the conduction band under visible light, which leads to the separation of electrons and holes. Meanwhile, phenol was adsorbed to  $\beta$ -CD (Fig. S9). b) Under the built-in electric field with electron-hole double transfer, plenty of electrons are quickly transferred to the NC nanotubes and react with oxygen to form a strongly oxidizing- $O_2^-$ , as shown in Eq. (6). c) Meanwhile, the double electron channel reduces the  $O_2$  in the water to produce  $H_2O_2$ , as shown in Eq. (7), considering that the conduction band potential is more negative than  $O_2/H_2O_2$  (0.68 eV vs. NHE). d) The holes are transferred to the  $\beta$ -CD/PANI. As the LUMO of CDP is more negative than those of  $O_2^{2-}/^1O_2$  (0.67 eV vs. NHE),  $h^+$  will react with  $O_2^{2-}$  to form  $^1O_2$ , as shown in Eq. (8). Certainly, holes can also directly oxidize phenol. e) Finally, with the synergistic effect of  $h^+$ ,  $^1O_2$ , and  $H_2O_2$ , the phenol in the water can be rapidly degraded (Eq. (9)).



#### 4. Conclusion

By electrostatically doping NC nanotubes and  $\beta$ -CD/PANI in the Ag<sub>3</sub>PO<sub>4</sub> ternary composite catalysts with a built-in electric field were constructed. The 3%CDP@Ag<sub>3</sub>PO<sub>4</sub>@NC had the best photocatalytic performance, which was mainly attributed to the minimum recombination rate of electrons and holes, the production of  $H_2O_2$  by oxygen reduction after electron transfer to NC, and the strong oxidation after hole transfer to CDP. At the same time, the doping of NC and CDP promoted more exposure of active crystal planes and improved the enrichment ability of materials for pollutants. These factors all enabled 3%CDP@Ag<sub>3</sub>PO<sub>4</sub>@NC to synergistically degrade pollutants very quickly. We believe that this study provides a new concept for efficient photocatalytic degradation of phenol, and also provides new insights for future photocatalysis.

#### CRedit authorship contribution statement

**Junwei Yuan:** Conceptualization, Methodology, Software. **Guan Wang:** Writing – reviewing & editing. **Cheng Zhang:** Data curation, Writing – original draft preparation. **Yuxiang Wang:** Software, Validation. **Liujun Yang:** Data curation, Software. **Miaomiao Li:** Data curation, Software. **Jianmei Lu & Hua Li:** Supervision.

#### Declaration of Competing Interest

The authors declare that they have no known competing financial interests or personal relationships that could have appeared to influence the work reported in this paper.

#### Acknowledgments

This work was financially supported by the NSF of China (21878199,

21938006), National Key Technology R&D Program (2020YFC1808401), Basic Research Project of Leading Technology in Jiangsu Province (BK20202012) and Priority Academic Program Development of Jiangsu Higher Education Institutions (PAPD).

#### Appendix A. Supporting information

Supplementary data associated with this article can be found in the online version at doi:10.1016/j.apcatb.2021.120892.

#### References

- [1] M.L. Marin, L. Santos-Juanes, A. Arques, A.M. Amat, M.A. Miranda, Organic photocatalysts for the oxidation of pollutants and model compounds, *Chem. Rev.* 112 (2012) 1710–1750.
- [2] L. Zhao, D. Xiao, Y. Liu, H. Xu, H. Nan, D. Li, Y. Kan, X. Cao, Biochar as simultaneous shelter, adsorbent, pH buffer, and substrate of *Pseudomonas citronellois* to promote biodegradation of high concentrations of phenol in wastewater, *Water Res.* 172 (2020), 115494.
- [3] L. Cheng, Q.J. Xiang, Y.L. Liao, H.W. Zhang, CdS-based photocatalysts, *Energy Environ. Sci.* 11 (2018) 1362–1391.
- [4] W. Wang, M.O. Tade, Z.P. Shao, Nitrogen-doped simple and complex oxides for photocatalysis: a review, *Prog. Mater. Sci.* 92 (2018) 33–63.
- [5] M. Wen, G. Li, H. Liu, J. Chen, T. An, H. Yamashita, Metal-organic framework-based nanomaterials for adsorption and photocatalytic degradation of gaseous pollutants: recent progress and challenges, *Environ. Sci. Nano* 6 (2019) 1006–1025.
- [6] S.S. Chen, T. Takata, K. Domen, Particulate photocatalysts for overall water splitting, *Nat. Rev. Mater.* 2 (2017) 17050.
- [7] J. Low, J. Yu, M. Jaroniec, S. Wageh, A.A. Al-Ghamdi, Heterojunction photocatalysts, *Adv. Mater.* 29 (2017), 1601694.
- [8] C. Gao, T. Wei, Y. Zhang, X. Song, Y. Huan, H. Liu, M. Zhao, J. Yu, X. Chen, A. Photoresponsive, Rutile TiO<sub>2</sub> heterojunction with enhanced electron-hole separation for high-performance hydrogen evolution, *Adv. Mater.* 31 (2019), e1806596.
- [9] Y. Lin, X. Wu, Y. Han, C.P. Yang, Y. Ma, C. Du, Q. Teng, H.Y. Liu, Y.Y. Zhong, Spatial separation of photogenerated carriers and enhanced photocatalytic performance on Ag<sub>3</sub>PO<sub>4</sub> catalysts via coupling with PPy and MWCNTs, *Appl. Catal. B* 258 (2019), 117969.
- [10] G. Wang, R. Huang, J. Zhang, J. Mao, D. Wang, Y. Li, Synergistic modulation of the separation of photo-generated carriers via engineering of dual atomic sites for promoting photocatalytic performance, *Adv. Mater.* (2021), e2105904.
- [11] S. Ji, Y. Qu, T. Wang, Y. Chen, G. Wang, X. Li, J. Dong, Q. Chen, W. Zhang, Z. Zhang, S. Liang, R. Yu, Y. Wang, D. Wang, Y. Li, Rare-earth single erbium atoms for enhanced photocatalytic CO<sub>2</sub> reduction, *Angew. Chem. Int. Ed.* 59 (2020) 10651–10657.
- [12] G. Wang, C.T. He, R. Huang, J. Mao, D. Wang, Y. Li, Photoinduction of Cu single atoms decorated on UiO-66-NH<sub>2</sub> for enhanced photocatalytic reduction of CO<sub>2</sub> to liquid fuels, *J. Am. Chem. Soc.* 142 (2020) 19339–19345.
- [13] Z. Yi, J. Ye, N. Kikugawa, T. Kako, S. Ouyang, H. Stuart-Williams, H. Yang, J. Cao, W. Luo, Z. Li, Y. Liu, R.L. Withers, An orthophosphate semiconductor with photooxidation properties under visible-light irradiation, *Nat. Mater.* 9 (2010) 559–564.
- [14] H.Y. Hu, Z.B. Jiao, H.C. Yu, G.X. Lu, J.H. Ye, Y.P. Bi, Facile synthesis of tetrahedral Ag<sub>3</sub>PO<sub>4</sub> submicro-crystals with enhanced photocatalytic properties, *J. Mater. Chem. A* 1 (2013) 2387–2390.
- [15] C. Li, P. Zhang, R. Lv, J. Lu, T. Wang, S. Wang, H. Wang, J. Gong, Selective deposition of Ag(3)PO(4) on monoclinic BiVO(4)(040) for highly efficient photocatalysis, *Small* 9 (2013) 3951–3956, 3950.
- [16] X. Guan, L. Guo, Cocatalytic effect of SrTiO<sub>3</sub> on Ag<sub>3</sub>PO<sub>4</sub> toward enhanced photocatalytic water oxidation, *ACS Catal.* 4 (2014) 3020–3026.
- [17] H.C. Zhang, H. Huang, H. Ming, H.T. Li, L.L. Zhang, Y. Liu, Z.H. Kang, Carbon quantum dots/Ag<sub>3</sub>PO<sub>4</sub> complex photocatalysts with enhanced photocatalytic activity and stability under visible light, *J. Mater. Chem.* 22 (2012) 10501–10506.
- [18] X.F. Yang, H.Y. Cui, Y. Li, J.L. Qin, R.X. Zhang, H. Tang, Fabrication of Ag<sub>3</sub>PO<sub>4</sub>-graphene composites with highly efficient and stable visible light photocatalytic performance, *ACS Catal.* 3 (2013) 363–369.
- [19] V. Vaiano, M. Matarangolo, J.J. Murcia, H. Rojas, J.A. Navio, M.C. Hidalgo, Enhanced photocatalytic removal of phenol from aqueous solutions using ZnO modified with Ag, *Appl. Catal., B* 225 (2018) 197–206.
- [20] S. Rojas, P. Horcajada, Metal-organic frameworks for the removal of emerging organic contaminants in water, *Chem. Rev.* 120 (2020) 8378–8415.
- [21] W. Jiang, W. Luo, R. Zong, W. Yao, Z. Li, Y. Zhu, Polyaniline/carbon nitride nanosheets composite hydrogel: a separation-free and high-efficient photocatalyst with 3D hierarchical structure, *Small* 12 (2016) 4370–4378.
- [22] S. Wang, Y. Wang, S.L. Zhang, S.Q. Zang, X.W.D. Lou, Supporting ultrathin ZnIn<sub>2</sub>S<sub>4</sub> nanosheets on Co/N-doped graphitic carbon nanocages for efficient photocatalytic H<sub>2</sub> generation, *Adv. Mater.* 31 (2019), e1903404.
- [23] Y. Li, C. Zhang, S. Ling, C. Ma, J. Zhang, Y. Jiang, R. Zhao, H. Li, J. Lu, Q. Zhang, Toward highly robust nonvolatile multilevel memory by fine tuning of the nanostructural crystalline solid-state order, *Small* 17 (2021), e2100102.

- [24] J. Shi, Y. Chen, Q. Wang, Y. Liu, Construction and efficient radical cation stabilization of cyclodextrin/aniline polypseudorotaxane and its conjugate with carbon nanotubes, *Adv. Mater.* 22 (2010) 2575–2578.
- [25] S.B. Wang, B.Y. Guan, X.W. Lou, Rationally designed hierarchical N-doped carbon@NiCo<sub>2</sub>O<sub>4</sub> double-shelled nanoboxes for enhanced visible light CO<sub>2</sub> reduction, *Energy Environ. Sci.* 11 (2018) 306–310.
- [26] Y. Bi, S. Ouyang, N. Umezawa, J. Cao, J. Ye, Facet effect of single-crystalline Ag<sub>3</sub>PO<sub>4</sub> sub-microcrystals on photocatalytic properties, *J. Am. Chem. Soc.* 133 (2011) 6490–6492.
- [27] E. Jung, H. Shin, B.H. Lee, V. Efremov, S. Lee, H.S. Lee, J. Kim, W. Hooch Antink, S. Park, K.S. Lee, S.P. Cho, J.S. Yoo, Y.E. Sung, T. Hyeon, Atomic-level tuning of Co-N-C catalyst for high-performance electrochemical H<sub>2</sub>O<sub>2</sub> production, *Nat. Mater.* 19 (2020) 436–442.
- [28] D.J. Martin, N. Umezawa, X.W. Chen, J.H. Ye, J.W. Tang, Facet engineered Ag<sub>3</sub>PO<sub>4</sub> for efficient water photooxidation, *Energy Environ. Sci.* 6 (2013) 3380–3386.
- [29] W. Kong, L. Huang, X. Quan, Z. Zhao, G. Li Puma, Efficient production of acetate from inorganic carbon (HCO<sub>3</sub><sup>-</sup>) in microbial electrosynthesis systems incorporating Ag<sub>3</sub>PO<sub>4</sub>/g-C<sub>3</sub>N<sub>4</sub> anaerobic photo-assisted biocathodes, *Appl. Catal. B* 284 (2021), 119696.
- [30] Y. Lin, C. Yang, S. Wu, X. Li, Y. Chen, W.L. Yang, Construction of built-In electric field within silver phosphate photocatalyst for enhanced removal of recalcitrant organic pollutants, *Adv. Funct. Mater.* 30 (2020), 2002918.
- [31] L. Zhao, Y.S. Hu, H. Li, Z. Wang, L. Chen, Porous Li<sub>4</sub> Ti<sub>5</sub> O<sub>12</sub> coated with N-doped carbon from ionic liquids for Li-ion batteries, *Adv. Mater.* 23 (2011) 1385–1388.
- [32] S. Chen, D.L. Huang, G.M. Zeng, W.J. Xue, L. Lei, P. Xu, R. Deng, J. Li, M. Cheng, In-situ synthesis of facet-dependent BiVO<sub>4</sub>/Ag<sub>3</sub>PO<sub>4</sub>/PANI photocatalyst with enhanced visible-light-induced photocatalytic degradation performance: synergism of interfacial coupling and hole-transfer, *Chem. Eng. J.* 382 (2020), 122840.
- [33] J.-X. Feng, S.-Y. Tong, Y.-X. Tong, G.-R. Li, Pt-like hydrogen evolution electrocatalysis on PANI/CoP hybrid nanowires by weakening the shackles of hydrogen ions on the surfaces of catalysts, *J. Am. Chem. Soc.* 140 (2018) 5118–5126.
- [34] H. Zhang, R. Zong, J. Zhao, Y. Zhu, Dramatic visible photocatalytic degradation performances due to synergetic effect of TiO<sub>2</sub> with PANI, *Environ. Sci. Technol.* 42 (2008) 3803–3807.
- [35] Z. Wang, X. Peng, C. Huang, X. Chen, W. Dai, X. Fu, CO gas sensitivity and its oxidation over TiO<sub>2</sub> modified by PANI under UV irradiation at room temperature, *Appl. Catal. B* 219 (2017) 379–390.
- [36] Q. Yao, Q. Wang, L. Wang, L. Chen, Abnormally enhanced thermoelectric transport properties of SWNT/PANI hybrid films by the strengthened PANI molecular ordering, *Energy Environ. Sci.* 7 (2014) 3801–3807.
- [37] Q. Yao, Q. Wang, L. Wang, L. Chen, Abnormally enhanced thermoelectric transport properties of SWNT/PANI hybrid films by the strengthened PANI molecular ordering, *Energy Environ. Sci.* 7 (2014) 3801–3807.
- [38] Q.H. Zhang, L. Gao, J.K. Guo, Effects of calcination on the photocatalytic properties of nanosized TiO<sub>2</sub> powders prepared by TiCl<sub>4</sub> hydrolysis, *Appl. Catal. B* 26 (2000) 207–215.
- [39] C. Gao, J. Wang, H. Xu, Y. Xiong, Coordination chemistry in the design of heterogeneous photocatalysts, *Chem. Soc. Rev.* 46 (2017) 2799–2823.
- [40] Z. Zhang, Y. Zhu, X. Chen, H. Zhang, J. Wang, A full-spectrum metal-free porphyrin supramolecular photocatalyst for dual functions of highly efficient hydrogen and oxygen evolution, *Adv. Mater.* 31 (2019), 1806626.
- [41] H. Wang, X. Wang, R. Chen, H. Zhang, X. Wang, J. Wang, J. Zhang, L. Mu, K. Wu, F. Fan, Promoting photocatalytic H<sub>2</sub> evolution on organic-inorganic hybrid perovskite nanocrystals by simultaneous dual-charge transportation modulation, *ACS Energy Lett.* 4 (2018) 40–47.
- [42] J. Jing, J. Yang, Z. Zhang, Y. Zhu, Supramolecular zinc porphyrin photocatalyst with strong reduction ability and robust built-in electric field for highly efficient hydrogen production, *Adv. Energy Mater.* 11 (2021), 2102217.
- [43] M.C. Wen, S.N. Song, Q.X. Liu, H.B. Yin, K. Mori, Y. Kuwahara, G.Y. Li, T.C. An, H. Yamashita, Manipulation of plasmon-induced hot electron transport in Pd/MoO<sub>3</sub>-x@ZIF-8: boosting the activity of Pd-catalyzed nitroaromatic hydrogenation under visible-light irradiation, *Appl. Catal. B* 282 (2021), 119511.
- [44] J.M. Lee, E.K. Mok, S. Lee, N.S. Lee, L. Debbichi, H. Kim, S.J. Hwang, A conductive hybridization matrix of RuO<sub>2</sub> two-dimensional nanosheets: a hybrid-type photocatalyst, *Angew. Chem. Int. Ed.* 55 (2016) 8546–8550.
- [45] L. Zhang, J. Ran, S.-Z. Qiao, M. Jaroniec, Characterization of semiconductor photocatalysts, *Chem. Soc. Rev.* 48 (2019) 5184–5206.
- [46] T.H. Gu, X. Jin, S.J. Park, M.G. Kim, S.J. Hwang, Molecular-level control of the intersheet distance and electronic coupling between 2D semiconducting and metallic nanosheets: establishing design rules for high-performance hybrid photocatalysts, *Adv. Sci.* 8 (2021), 2004530.
- [47] S. Xiao, D. Zhang, D. Pan, W. Zhu, P. Liu, Y. Cai, G. Li, H. Li, A chloroplast structured photocatalyst enabled by microwave synthesis, *Nat. Commun.* 10 (2019) 1–10.
- [48] J. Moan, E. Wold, Detection of singlet oxygen production by ESR, *Nature* 279 (1979) 450–451.
- [49] J. Byun, W. Huang, D. Wang, R. Li, K.A. Zhang, CO<sub>2</sub>-Triggered switchable hydrophilicity of a heterogeneous conjugated polymer photocatalyst for enhanced catalytic activity in water, *Angew. Chem. Int. Ed.* 57 (2018) 2967–2971.